GEOPHYSICS, VOL. 91, NO. 1 (NOVEMBER-DECEMBER 2025); P. WA1–WA9, 7 FIGS., 3 TABLES.
10.1190/GEO2024-0887.1

Effect of the fractal distribution of the radius of CO_2 patches on the ultrasonic velocity and attenuation of tight rocks

Lin Zhang[1], Guangdong Chen[1], Jing Ba[1], José M. Carcione[2], and Bingbing Yang[1]

ABSTRACT

Carbon dioxide (CO_2) injection is currently being carried out to improve hydrocarbon recovery and reduce carbon emissions. In this study, we measure the ultrasonic velocity and attenuation during supercritical CO_2 injection into three oil-saturated tight rock samples (one sandstone and two carbonates). The experiments indicate that P-wave velocity is very sensitive to the pore-fluid substitutions, whereas the shear modulus and velocity are independent of it. Using the classical Gassmann model, the bulk moduli at different CO_2 saturations obtained from the data exceed the Gassmann-Voigt upper bound, which is attributed to elastic stiffening. To model the P-wave velocity and attenuation, we use a poroelastic (mesoscopic-loss) model with a fractal distribution of the radius of the CO_2 patches, and find that this model performs better than the White model, which is based on a single radius.

INTRODUCTION

Carbon dioxide (CO_2), an important component of the earth's atmosphere, has attracted considerable attention in recent years due to its crucial role in global warming and climate change (Masson-Delmotte et al., 2022). Carbon capture and storage, which involves the injection of CO_2 into subsurface formations or hydrocarbon reservoirs, is considered an optimal strategy to mitigate this problem (Schrag, 2007; Alemu et al., 2013; Vasco et al., 2019). To achieve effective long-term storage of subsurface CO_2, time-lapse seismic methods have been used to map the movement of CO_2 in the subsurface and estimate CO_2 saturation (Arts et al., 2004; Daley et al., 2008; Chadwick et al., 2010; Caspari et al., 2011; Li et al., 2013). However, CO_2 injection creates a complex system of CO_2, pore fluid, and mineral grains in the rock (Thomas and Benson, 2005; Lei and Xue, 2009; Yu et al., 2019), especially under additional temperature and pressure conditions (Yang et al., 2022, Deng et al., 2023, 2024; Li et al., 2024). This complicates the understanding of the relationship between CO_2 saturation/spatial distribution and elastic wave velocity/attenuation. This complexity poses a major challenge for the time-lapse seismic monitoring of CO_2 storage in subsurface reservoirs.

CO_2 injection can lead to the dissolution or precipitation of mineral grains (Le Guen et al., 2007; Vialle and Vanorio, 2011; Alam et al., 2014; Delle Piane and Sarout, 2016; Foroutan et al., 2021), changes in pore fluid properties (Batzle and Wang, 1992; Han et al., 2012), and changes in pore structure (Jiang et al., 2016; Yin et al., 2016; Cheng et al., 2020; Yang et al., 2023). Eventually, these changes may affect the porosity and elastic properties of the rock, which have been investigated through a series of laboratory tests. Wang and Nur (1989) conduct pioneering work measuring the P- (V_P) and S-wave (V_S) velocities of eight sandstones saturated with n-hexadecane before and after CO_2 flooding. Given that CO_2 injection gradually displaces pore fluid, the elastic properties of a partially saturated rock can be described by Gassmann's (1951) equation, incorporating the fluid bulk modulus from Wood's (1941) equation (GW bound). Their findings indicate that the results of the GW bound closely agreed with the measurements. Xue and Ohsumi (2004) and Shi et al. (2007) investigate the changes in V_P of water-saturated Tako sandstone under different types of CO_2 flooding scenarios, comparing their measurements with predictions estimated from the GW bound. Siggins (2006) and Siggins et al. (2010) perform experimental investigations of P-wave velocity and attenuation in synthetic and field sandstone samples during CO_2 injection. Lebedev et al. (2013) measure the acoustic velocity of five shaley sandstones from the Otway Basin during supercritical CO_2 ($scCO_2$) displacement, revealing a transition from the GH bound to the GW bound at varying $scCO_2$ saturations (The effective bulk

Manuscript received by the Editor 3 December 2024; revised manuscript received 14 February 2025; published ahead of production 22 March 2025; published online 18 August 2025.
[1]Hohai University, School of Earth Sciences and Engineering, Nanjing, China. E-mail: zlin@hhu.edu.cn; cgd010111@163.com; jba@hhu.edu.cn (corresponding author); bbyang@hhu.edu.cn.
[2]Hohai University, School of Earth Sciences and Engineering, Nanjing, China and National Institute of Oceanography and Applied Geophysics — OGS, Trieste, Italy. E-mail: jose.carcione@gmail.com.

modulus of a partially saturated rock is estimated from the Hill (1963) equation by using the bulk modulus of each phase obtained with the Gassmann equation.) Kitamura et al. (2014) inject CO_2 into a porous sandstone under in situ pressure and temperature conditions, and monitor the changes in V_P and V_S with saturation. Mohapatra et al. (2019) experimentally measure the ultrasonic velocity of Tuscaloosa sandstone during sequential displacement of pore fluids (brine, oil, and CO_2), and analyze the applicability of the Gassmann equation in rocks saturated with different fluid mixtures.

It is known that the elastic properties of partially saturated rocks are influenced not only by saturation levels but also by pore fluid distribution (Cadoret et al., 1995; Müller et al., 2010; Ba et al., 2017; Li et al., 2020; Liu et al., 2021; Sun et al., 2022). Xue and Lei (2006) measure the V_P of water-saturated sandstones during CO_2 injection, demonstrating that P-wave velocity tomograms obtained from differential seismic tomography were associated with CO_2 migration, which was governed by the heterogeneity of pore distribution. Using the same experimental method, Lei and Xue (2009) find that the White and Dutta and Odé (1979) model align well with the measured velocity and attenuation at various CO_2 saturations, under the assumption that patch sizes are uniform. They suggested that CO_2 injection might create CO_2 patches of varying sizes within the formation, potentially exhibiting a fractal distribution pattern. This conclusion was corroborated by Zhang et al. (2015), who illustrated the distribution of CO_2 and brine in porous sandstone using computed tomography (CT) images during CO_2/brine injection and estimated the fractal dimension of the P-wave modulus based on these images. In addition, they found that the predictions of the continuous random patchy saturation model (Toms et al., 2007; Müller et al., 2008) were consistent with their measurements. Furthermore, Zhang et al. (2017) compare the CO_2 distributions in one sandstone and one tuff during CO_2 injection and find that the distribution in the former was more heterogeneous during drainage. Yun and Song (2022) conduct experimental investigations of pore fluid substitutions of CO_2 and H_2O in Berea sandstone and discuss the effects of pore fluid distribution on V_P.

Pore fluids with gas mixture affect both elastic and electrical properties in fractured rocks (Liu et al., 2022; Sheng et al., 2024). Because CO_2 injection also affects the electrical property of the rock, it can provide additional and complementary information to better understand how CO_2 injection affects seismic attributes. Alemu et al. (2013) measure the electrical resistivity and ultrasonic velocities of reservoir rock during the imbibition and drainage of CO_2, as well as simultaneously mapping fluid distribution using an X-ray CT scanner. They compared the measured velocity with the mode prediction of GW, using the Gassmann equation with fluid bulk modulus from the Voigt equation (GV), and Brie et al. (1995). Their results demonstrated how subcore scale heterogeneities and fluid distribution patterns impact elastic and electrical properties. Kim et al. (2011) report the changes in resistivity and V_P during CO_2 injection into water-saturated sandstone. Their findings indicated that the saturation estimated from resistivity can clarify the relationship between CO_2 saturation and V_P. Based on this conclusion, Falcon-Suarez et al. (2018) remark that the measured ultrasonic P-wave velocities and attenuations are influenced by CO_2 distribution and squirt flow effects. In a subsequent study on the elastic behavior of CO_2-brine saturated fractured rocks, Falcon-Suarez et al. (2020) measure ultrasonic P- and S-wave velocity and attenuation and electrical resistivity of synthetic fractured sandstone. They analyzed the dependence of these measurements on CO_2 saturation using the model proposed by Jin et al. (2018), which combines patchy fluid distribution and the squirt flow phenomenon for partially saturated anisotropic rocks. To further understand the relationship of CO_2 saturation and elastic wave velocity and attenuation at seismic frequencies, Nakagawa et al. (2013) conduct seismic measurements of sandstones in a frequency band of 1–2 kHz during $scCO_2$ injection and compare their measurements with the predicted results from Gassmann and White models. Mikhaltsevitch et al. (2014) experimentally measure the elastic moduli of sandstone flooded with $scCO_2$ at seismic (0.1–100 Hz) and ultrasonic (approximately 0.5 MHz) frequencies. They found that the Gassmann model has the ability to interpret the measurements. Agofack et al. (2018) investigate the effect of CO_2 on V_P and V_S of Castlegate sandstone at seismic (1–155 Hz) and ultrasonic frequencies (approximately 500 kHz). They found that P-wave velocity dispersion and attenuation can be described by the Cole and Cole (1941) model.

The effects of rock-pore fluid-CO_2 interactions on the elastic properties were not considered in the preceding studies. However, understanding these interactions is crucial, particularly in the contexts of CO_2 sequestration, hydrocarbon recovery, and other subsurface applications. Several studies have investigated how these interactions influence the mechanical and elastic properties of reservoir rocks. Chapman et al. (2021) conduct CO_2 exsolution experiments on a Berea sandstone sample, demonstrating that numerical simulations incorporating CO_2 saturation distributions derived from X-ray CT scans closely matched measurements of attenuation and modulus dispersion across frequencies ranging from 0.1 to 1000 Hz. Hangx et al. (2013, 2015) investigate the effect of CO_2/brine/rock interactions on the mechanical behavior of sandstone samples. Their research highlighted that prolonged exposure to CO_2-rich brine could lead to mineral dissolution and precipitation reactions, which weaken the rock matrix. This alteration, in turn, affects the elastic moduli and strength of the rock. Falcon-Suarez et al. (2024) measure the elastic and electrical properties of three sandstone samples with similar mineralogy but different physical properties using CO_2 flow-through tests. Their findings revealed that CO_2 distribution correlates with the clay fraction, CO_2-clay chemical interactions, and the porosity of the samples. In addition, they showed that the measured P-wave velocity (V_P) during drainage was well described by the White and Dutta-Odé model, whereas the measurements during imbibition were adequately explained by the GW bound.

CO_2 injection has proven to be an effective method of enhancing oil and gas recovery in tight reservoirs that have significant resource potential. Most previous studies concentrate on injecting CO_2 into water-saturated high porosity sandstone, but few studies pay attention to elastic wave velocity and attenuation of oil-saturated tight rocks during CO_2 injection. In this work, we selected three tight rock samples — two carbonate and one sandstone — to measure ultrasonic wave velocity and attenuation at varying $scCO_2$ saturation. The effects of CO_2 saturation and distribution were then analyzed according to a theoretical model of partially saturated rocks proposed by Zhang et al. (2022). Finally, we compared the predicted result of the White model and measurements.

EXPERIMENTS

Samples

Two tight carbonate samples (Met 16 and Met 17) from the Metajan district were prepared as cylinders with dimensions of

43.3/50.0 mm in length and 38.02/38.03 mm in diameter, respectively. Both samples primarily consist of calcite (>95%) and clay (<5%) (Yu et al., 2014; Zhang et al., 2024). In addition, one tight sandstone sample (2–8) from Member 7 of the Yanchang Formation in the Ordos Basin has a length of 36.25 mm and a diameter of 25.19 mm. Its composition, determined from X-ray diffraction (XRD) analysis, includes quartz (54.88%), potassium feldspar (9.74%), plagioclase (21.87%), calcite (1.96%), iron dolomite (1.97%), dolomite (3.16%), siderite (1.07%), and clay (5.35%). The physical properties of the samples are provided in Table 1. The thin section of sample 2–8 (Figure 1) shows that the rock particles have good sorting and roundness (subangular), and contain a number of pores and microcracks.

Experimental procedure

To investigate the effect of CO_2 injection on elastic properties of the oil-saturated samples, we conducted ultrasonic experiments under varying CO_2 saturation using an experimental apparatus shown in Figure 2. The procedure consisted of the following steps: (1) The samples underwent an oil-salt washing treatment, and were placed in a constant temperature chamber and dried to a constant weight at 105 ± 2°C. (2) The cold-cut samples were positioned in a holder, and the confining pressure (P_c) was increased to 20 MPa using a control unit. Simultaneously, a heating device raised the chamber temperature (T) to 35°C, and CO_2 was injected from both ends through the pore pressure control unit, and the pore pressure (P_p) was subsequently increased to 9 MPa. Throughout the injection process, real-time monitoring of gas volume changes occurred, and the sample was considered fully saturated when the injected gas volume no longer increased. These conditions were maintained for 4 h. Then, the ultrasonic P- and S-wave velocities and attenuation were measured using the pulse transmission method. (4) The samples were then removed from the holder and subjected to oil saturation by vacuum extraction and pressure application until their weight stabilized. The fully oil-saturated samples were then returned to the holder, where the same experimental conditions as in the step (3) were applied to measure the P- and S-wave velocities and attenuation. (5) Because the pressure at the outlet is lower than the critical pressure of $scCO_2$ (7.39 MPa), the phase at the outlet may turn to gas during the oil displacement process, resulting in some oil loss and affecting the accurate calculation of the oil saturation of the samples. Therefore, this experiment first used nitrogen gas for displacement at the room temperature and a constant pore pressure of 1.5 MPa. A measuring tube was installed at the outlet to quantify the volume of oil displaced. After calculating the oil saturation of the samples, the outlet was sealed, and $scCO_2$ was then injected from both ends. Under the high-pressure conditions of $scCO_2$, the volume of nitrogen is significantly compressed by the CO_2, which does not affect the CO_2 saturation. Once the injected gas volume stabilized, the sample was considered saturated. These conditions were maintained for 4 h before measuring the P- and S-wave velocities and attenuation. This procedure was repeated sequentially to measure the P- and S-wave velocities and attenuation of the samples with varying $scCO_2$ saturations. The properties of the pore fluids used in the tests are provided in Table 2.

EXPERIMENTAL RESULTS

The experimental results of three samples as a function of $scCO_2$ saturation are shown in Figure 3. Figure 3a shows that the V_P of samples Met 16 and Met 17 decrease with increasing $scCO_2$ saturation. A similar trend has been reported by Alemu et al. (2013) and Yun and Song (2022). The corresponding V_S increase slowly with increasing saturation (Figure 3b), which contrasts with the observed V_P trend. This behavior is primarily attributed to the $scCO_2$, having a lower density than oil. In contrast, the V_P of sample 2–8 first

Table 1. Physical properties of the samples.

Sample	Met 16	Met 17	2–8
Porosity ϕ (%)	8.384	4.638	10.345
Dry-rock density ρ_{dry} (kg/m^3)	2428.9	2553.4	2340
Permeability κ (mD)	2.612	0.398	0.096

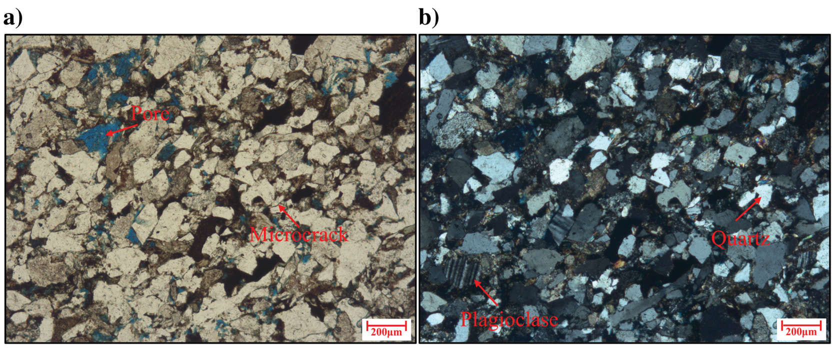

Figure 1. Thin section of sample 2–8 under orthogonal (a) single and (b) polarization images.

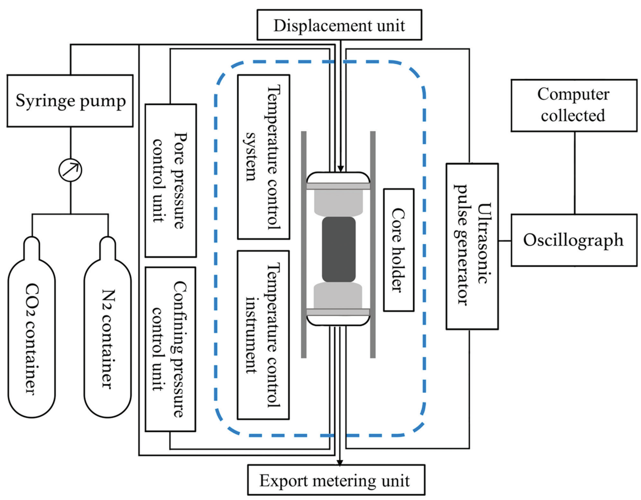

Figure 2. Diagram of the apparatus with ultrasonic P- and S-wave measurement system (modified from Zhang et al. 2024).

increases and then decreases, indicating a nonlinear behavior, reflecting complex interactions. Falcon-Suarez et al. (2024) report similar effects, and suggest that this behavior arises from a decrease in effective mobility, leading to stronger velocity dispersion at lower $scCO_2$ saturation. Sample 2–8, which has the highest porosity, shows the most significant decrease in V_P, followed by samples Met 16 and Met 17. This behavior is consistent with the sample porosities.

Table 2. Physical properties of the pore fluids at P_p = 9 MPA and T = 35°C.

Fluid type	Density (kg/m^3)	Bulk modulus (GPa)	Viscosity (cP)
$scCO_2$[3]	662.13	0.0503	0.0514
Oil	801.7	1.6234	2.0

[3]The density, viscosity, and sound velocity of $scCO_2$ are obtained from the National Institute for Standards and Technology (Lemmon et al., 2012), and the bulk modulus is calculated from density and sound velocity.

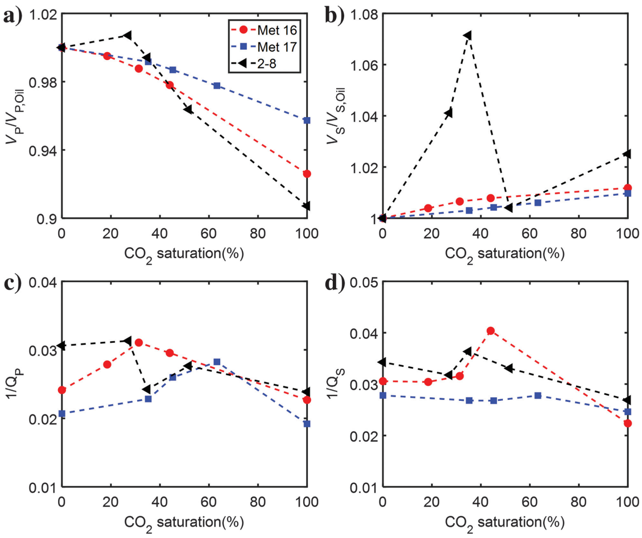

Figure 3. Experimental ultrasonic P- and S-wave velocities and attenuation of samples Met 16, Met 17, and 2–8 as a function of $scCO_2$ saturation, where the velocities are normalized with respect to the corresponding values of the oil-saturated samples ($V_{P,oil}$ = 5405, 6030, 4264 m/s and $V_{S,oil}$ = 2809, 3005, 2466 m/s).

The corresponding P- and S-wave attenuations ($1/Q_P$ and $1/Q_S$) are shown in Figure 3c and 3d, respectively. For sample Met 16, $1/Q_P$ is highest at $scCO_2$ saturation of 31.4%, whereas $1/Q_S$ peaks at $scCO_2$ saturation of 44%. In the case of sample Met 17, $1/Q_P$ and $1/Q_S$ reach their maximum values at $scCO_2$ saturation of 63.3%. For sample 2–8, attenuation $1/Q_P$ and $1/Q_S$ have maxima reaching at saturations of 27.1% and 35%, respectively. This complex attenuation behavior may reflect localized zones of higher or lower $scCO_2$ concentration, leading to uneven seismic energy dissipation and potentially influencing wave propagation (Papageorgiou et al., 2018). It is also noted that the attenuation peak shifts to higher $scCO_2$ saturation as porosity increases. The attenuation at full oil saturation shows a correlation with porosity.

DATA ANALYSIS AND DISCUSSION

Effect of the pore fluid on the elastic moduli

Figure 4 shows the effect of the pore fluid, where the elastic moduli are calculated from the experimental V_P, V_S, and $\rho = \rho_{dry} + \phi(\rho_o S_o + \rho_{CO_2} S_{CO_2})$, where ρ_{dry} is the dry-rock density; ρ_o and ρ_{CO_2} are the oil and CO_2 densities, respectively; and S_o and S_{CO_2} are the corresponding saturations. Figure 4b shows that the shear moduli of the rock fully saturated with oil and $scCO_2$ are nearly identical. This indicates that the CO_2 injection does not change the shear moduli of the skeleton. A similar behavior has been reported (Lebedev et al., 2013; Yun and Song, 2022). At $P_p = 9$MPa and T = 35°C, the bulk modulus (viscosity) of $scCO_2$ is in the same order of magnitude as that of air, which leads to minimal differences in experimental measurements between dry and $scCO_2$-saturated rocks. This conclusion can also be found in Figure 10 of Lebedev et al. (2013). It is therefore reasonable to assume that fluid dispersion effects in the $scCO_2$-saturated samples in this work can be considered negligible. Consequently, we assume that the dry-rock elastic moduli can be estimated from measurements of fully CO_2-saturated rocks by applying the inverse Gassmann equation. For samples Met 16, Met 17, and 2–8, the inverted dry-rock bulk/shear moduli are 35.31/20.07, 54.3/23.78, and 15.4/15.3 GPa, respectively. These values are incorporated into the GW and GV bounds. The grain bulk/shear moduli of samples Met 16 and Met 17 are 76.8/32 GPa, corresponding to the elastic moduli of calcite. The bulk/shear Voigt-Reuss-Hill averages of sample 2–8 are 46.8/33.2 GPa (Mavko et al., 2009), based on a mineralogical composition determined by XRD analysis.

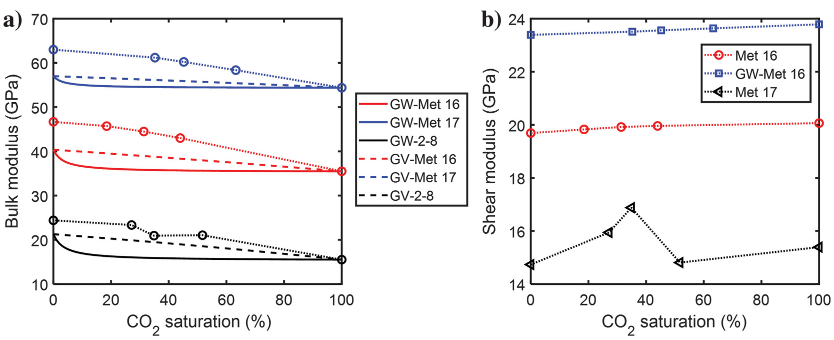

Figure 4. (a) Bulk and (b) shear moduli of samples Met 16, Met 17, and 2–8 as a function of CO_2 saturation. The dotted lines with circles are the measurements, and the solid and broken lines are the predicted values by the GW and GV bounds.

Figure 4a shows that the experimental bulk moduli exceed the predictions of the upper (i.e., GV) bound, with the discrepancy increasing as the CO_2 saturation decreases. This behavior differs from previous results for high-porosity sandstone (e.g., Lebedev et al., 2013; Lei and Xue, 2009; Yun and Song, 2022), suggesting that when the rock is saturated with oil, part of it saturates the microcracks and the stiffness of the rock skeleton increases (Mavko and Jizba, 1991). Furthermore, the presence of local fluid flow resulting from fabric heterogeneities contributes to this discrepancy, which is not accounted for in this study.

The effect of pore fluid distribution

To investigate the effect of the pore fluid distribution, we use a fractal distribution of the size and volume fractions of the CO_2 fluid patches (Zhang et al., 2022) into a fully oil-saturated medium (or host). The corresponding equations of wave propagation can be found in Appendix A.

In this model, the CO_2 patches are assumed to follow a self-similar distribution with

$$v_{\mathrm{I}} = 1 - \left(\frac{r_{\min}}{r_{\max}}\right)^{D_E - D_f}, \tag{1}$$

where v_{I} is the inclusion volume fraction, which is equal to the $scCO_2$ saturation; $r_{\max}$ and $r_{\min}$ are the maximum and minimum inclusion radii, respectively;$D_E = 3$ is the Euclidean dimension; and D_f is the fractal dimension ($2 < D_f < 3$).

Figure 5a shows that the velocity does not depend of the fractal dimension at ultrasonic frequencies (i.e., $f = 10^6$ Hz) because the CO_2 modulus is much smaller than that of oil. In contrast, the velocity shows significant changes with the range of the inclusion radii (r), as shown in Figure 5b. Zhang et al. (2015) report that the relation between the fractal dimension D_f and saturation is nonunique. In what follows, we assume $D_f = 2.65$ and the distribution range of the inclusion radius is treated as a fitting parameter, which change as S_{CO_2} varies (Zhang et al., 2022).

Because the elastic stiffening of the skeleton, described previously, cannot be described by this model, we assume that the dry-rock shear modulus is a constant, and consider the dry-rock bulk modulus a fitting parameter. Figure 6 compares the measurements of samples Met 16, Met 17 and 2–8 and the theoretical results. The inverted dry-rock bulk moduli are provided in Table 3. Note that these moduli for samples Met 16 and Met 17 increase with decreasing S_{CO_2}, whereas those of sample 2–8 increase initially and then decrease. These moduli are input to the GW, GV, and Gassmann-Brie equations. (In the Brie model Brie et al. [1995] model, the effective fluid modulus is $K_f = (K_{\mathrm{oil}} - K_{CO_2})(1 - S_{CO_2})^n + K_{CO_2}$). Figure 6a, 6c, and 6e shows that the theoretical V_{P} agrees with the measurements for the distribution ranges of the CO_2 patches radii provided in Table 3. The radii of the CO_2 patches increase as S_{CO_2} increases. The distribution range of radii for samples Met 17 and 2–8 differs noticeably at $S_{CO_2} = 35\%$. This indicates that the pore fluid distribution is affected by the rock heterogeneity (Zhang et al., 2017). This means that the ultrasonic attenuation and velocity strongly depends on CO_2 saturation and inclusion radii. Although V_{P} obtained with the Gassmann-Brie equation (n = 1.8, 1.8, and 1.4 for samples Met 16, Met 17, and 2–8, respectively) shows a good agreement with the measurements, it does not provide detailed information on the distribution of CO_2 patches. Moreover, the measurements are within the GW and GV bounds.

Figure 6b, 6d, and 6e shows that the predicted $1/Q_{\mathrm{P}}$ are smaller than measurements, which may be attributed attenuation associated with the skeleton (Tisato and Quintal, 2013; Kuteynikova et al., 2014), as well as attenuation due to fabric heterogeneities (Ba et al., 2017; Zhang et al., 2021). For samples Met 16 and Met 17, the theoretical $1/Q_{\mathrm{P}}$ follow the same trend as those of the measurements. The predicted and measured $1/Q_{\mathrm{P}}$ of sample Met 16 have a maximum at the same saturation. In contrast, the predicted $1/Q_{\mathrm{P}}$ of sample 2–8 differs in trend from the measurements.

Comparison with the White model

In previous studies (Carcione et al., 2003; Lei and Xue, 2009; Nakagawa et al., 2013; Falcon-Suarez et al., 2024), the White model has been extensively used to assess the effect of pore fluids on wave attenuation, generally assuming a constant patch radius. Carcione et al. (2018) use the White mesoscopic-loss model with normal, Rayleigh, and uniform distributions of patch sizes. The radius of the CO_2 patches (denoted by a) can be estimated by fitting the experimental data with the White model using a least-squares regression. Figure 7 shows that this model performs well with a = 0.62, 0.17, and 0.18 mm for samples Met 16, Met 17, and 2–8, respectively. Here, a can be considered as an effective radius, approximating the actual pore fluid distribution, and its value is within the distribution range (see Table 3). However, Figure 7b, 7d, and 7f shows that the theoretical $1/Q_{\mathrm{P}}$ performs worse than the proposed model in this work, particularly for sample 2–8.

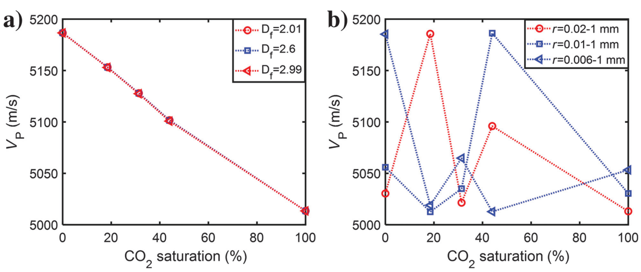

Figure 5. (a) Theoretical V_{P} at ultrasonic frequencies as a function of $scCO_2$ saturation with varying D_f and (b) distribution range of the inclusion radii, according to the parameters of sample Met 16.

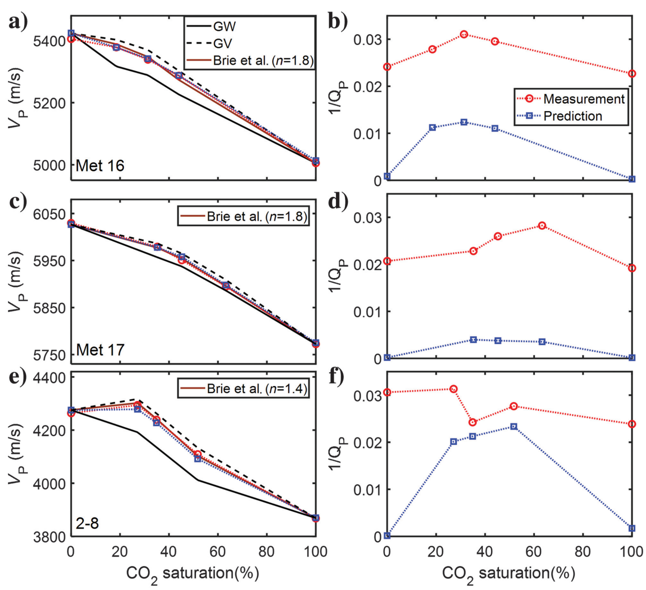

Figure 6. (a, c, and e) P-wave velocity and (b, d, and f) attenuation of samples Met 16, Met 17, and 2–8, respectively, as a function of $scCO_2$ saturation. The dotted lines with circles are the measurements, the dotted lines with squares are the theoretical results of Zhang et al. (2022), the brown line corresponds to the Brie model, and the solid and broken lines are the GW and GV bounds.

Table 3. Inverted dry-rock bulk moduli and distribution range of the inclusion radii of samples Met 16, Met 17, and 2–8.

			Met 16		
S_{CO_2} (%)	100	44	31.4	18.5	0
K_b (GPa)	35.31	41	42.6	43.2	43.27
r	0.06–3 mm	0.048–3 mm	0.03–3 mm	0.024–3 mm	—
			Met 17		
S_{CO_2} (%)	100	63.3	45.2	35.2	0
K_b (GPa)	54.3	57.8	59.4	60	61
r	0.03–3 mm	0.024–3 mm	0.024–3 mm	0.019–3 mm	—
			2–8		
S_{CO_2} (%)	100	51.7	35	27.1	0
K_b (GPa)	15.3	18	20.4	21.5	19
r	0.012–1.5 mm	0.075–1.5 mm	0.006–1.5 mm	0.0047–1.5 mm	—

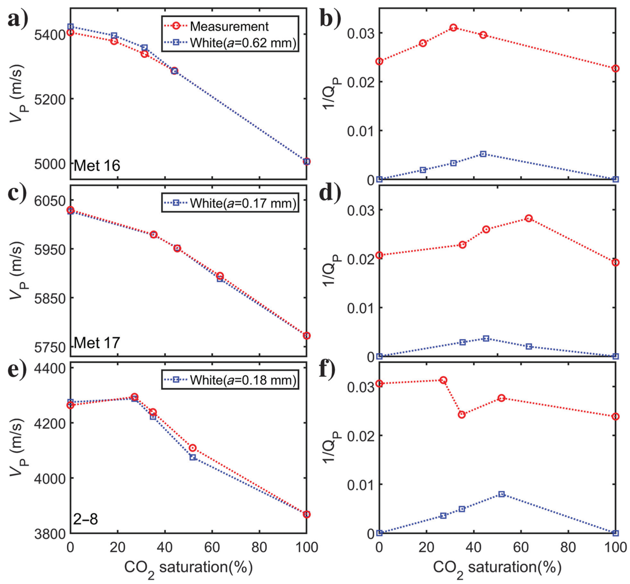

Figure 7. (a, c, and e) P-wave velocity and (b, d, and f) attenuation of samples Met 16, Met 17, and 2–8, respectively, as a function of $scCO_2$ saturation. The dotted lines with circles are the measurements, and the dotted lines with squares are the results of the White model with a single CO_2 patch radius.

CONCLUSION

We conducted experiments to measure the ultrasonic velocity and attenuation of oil-saturated tight rocks during CO_2 injection. The experimental data show that the P-wave velocities decrease significantly with increasing saturation, whereas the S-wave velocities show only a minimal change. This indicates that the elastic properties of the rock skeleton remain largely unchanged during injection. We also found a phenomenon of elastic stiffening due to oil trapped in the cracks, causing the classical Gassmann model to fail in accurately describing the measurements. Comparisons with theoretical models show that the velocity and attenuation of P waves depend on saturation and a fractal distribution range of the CO_2 patch radii. We find that this range decreases with increasing saturation. Combining laboratory measurements with a proper theoretical model provides valuable insights for estimating CO_2 saturation and patch sizes from seismic time-lapse data due to fluid injection. This approach can also provide more inferences and valid scenarios on pore properties from measurements to explain the effects on seismic velocities and attenuation. Based on these results, several follow-up research pieces will address: (1) the effects of CO_2 injection on rock-physical properties for different rock types, and as a function of temperature and pressure; (2) the influence of rock microstructure on the macroscopic physical properties during CO_2 injection; and (3) the improvement of theoretical models to better account for the complex fluid-rock interactions in tight reservoirs.

ACKNOWLEDGMENTS

This work was funded by the National Natural Science Foundation of China (Nos. 42104110, 42174161, 12334019, and 42404120), the Jiangsu Natural Science Foundation (No. BK20210379), and the China Postdoctoral Science Foundation (No. 2022M720989). We would like to thank the journal editors (A. Guitton, C. Farquharson) and two reviewers for their constructive feedbacks.

DATA AND MATERIALS AVAILABILITY

Data associated with this research are available and can be obtained by contacting the corresponding author.

APPENDIX A

WAVE PROPAGATION OF PARTIALLY SATURATED ROCKS WITH A FRACTAL DISTRIBUTION OF FLUID PATCHES

The corresponding equations for wave propagation are (Zhang et al., 2022)

$$
\begin{aligned}
&(N+NZ\phi_0 \mathrm{d}S)\nabla^2\mathbf{u}+(A+N)\nabla e+(A_\mathrm{d}+NZ)\phi_0\mathrm{d}S\nabla e\\
&+Q_\mathrm{H}\phi_0 S\nabla(\xi_\mathrm{H}+\zeta\phi_0\mathrm{d}S)\\
&+R_\mathrm{H}\left(\frac{Q_\mathrm{I}}{K_\mathrm{f}^\mathrm{I}}-\frac{Q_\mathrm{I}}{K_\mathrm{s}}-1\right)\phi_0\mathrm{d}S\nabla\xi_\mathrm{H}+Q_\mathrm{I}\phi_0\mathrm{d}S\nabla(\xi_\mathrm{I}-\phi_0 S\zeta)\\
&=\rho_{00}\ddot{\mathbf{u}}+(\rho_{00}Z-\rho_\mathrm{s}-\rho_{02})\phi_0\mathrm{d}S\ddot{\mathbf{u}}+\rho_{01}\phi_0 S\ddot{\mathbf{U}}_\mathrm{H}\\
&+\rho_{01}\phi_0^2 ZS\mathrm{d}S\ddot{\mathbf{U}}_\mathrm{H}+\rho_{02}\phi_0\mathrm{d}S\ddot{\mathbf{U}}_\mathrm{I}\\
&+\frac{\phi_0^2 S\eta_\mathrm{f}^\mathrm{H}}{\kappa_\mathrm{H}}(\dot{\mathbf{u}}-\dot{\mathbf{U}}_\mathrm{H})+\frac{\phi_0^3 S\eta_\mathrm{f}^\mathrm{H}}{\kappa_\mathrm{H}}Z\mathrm{d}S(\dot{\mathbf{u}}-\dot{\mathbf{U}}_\mathrm{H})+\frac{\phi_0^2\eta_\mathrm{f}^\mathrm{I}\mathrm{d}S}{\kappa_\mathrm{H}}(\dot{\mathbf{u}}-\dot{\mathbf{U}}_\mathrm{I}),
\end{aligned}
\tag{A-1a}
$$

$$
\begin{aligned}
&Q_\mathrm{H}\nabla e+R_\mathrm{H}\nabla(\xi_\mathrm{H}+\zeta\phi_0\mathrm{d}S)+\frac{R_\mathrm{H}}{\phi}(\nabla\xi_\mathrm{H}-\nabla e)\phi_0\mathrm{d}S\\
&=\left(1+\frac{R_\mathrm{H}}{S}\left(\frac{1}{K_\mathrm{f}^\mathrm{H}}-\frac{1}{K_\mathrm{s}}\right)\mathrm{d}S\right)\left(\rho_{01}\ddot{\mathbf{u}}+\rho_{11}\ddot{\mathbf{U}}_H-\frac{\phi_0\eta_\mathrm{f}^\mathrm{H}}{\kappa_\mathrm{H}}(\dot{\mathbf{u}}-\dot{\mathbf{U}}_\mathrm{H})\right),
\end{aligned}
\tag{A-1b}
$$

$$Q_\mathrm{I}\nabla e + R_\mathrm{I}\nabla(\xi_\mathrm{I} - \phi_0 S\zeta) = \rho_{02}\ddot{\mathbf{u}} + \rho_{22}\ddot{\mathbf{U}}_\mathrm{I} - \frac{\phi_0\eta_\mathrm{f}^\mathrm{H}}{\kappa_\mathrm{H}}(\dot{\mathbf{u}} - \dot{\mathbf{U}}_\mathrm{I}), \tag{A-1c}$$

$$(Q_\mathrm{H}e + R_\mathrm{H}(\xi_\mathrm{H} + \zeta\phi_0 \mathrm{d}S)) - (Q_\mathrm{I}e + R_\mathrm{I}(\xi_\mathrm{I} - \phi_0 S\zeta)) = \frac{1}{3}r^2\phi_0^2 S\left(\frac{\rho_\mathrm{f}^\mathrm{H}}{\phi_0}\ddot{\zeta} + \frac{\eta_\mathrm{f}^\mathrm{H}}{\kappa_\mathrm{H}}\dot{\zeta}\right), \tag{A-1d}$$

where $\mathbf{u}$ is the solid displacement. Here, $\mathbf{U}_\mathrm{H}$ and $\mathbf{U}_\mathrm{I}$ are the fluid displacements of the two pore phases saturated by oil and $scCO_2$, respectively; ξ_H (S) and ξ_I (dS) are the corresponding fluid strains (volume fractions); η_f^H and η_f^I are the viscosities of the host and inclusion fluids, respectively; and ρ_f^H is the fluid density of the host fluid. Moreover, the scalar ζ denotes the fluid strain increment between the two pore phases; K_s and ρ_s are the grain bulk modulus and density, respectively; K_b and G_b are the dry-rock bulk and shear moduli, respectively; κ_H is the permeability of the skeleton; and ϕ_0 is the porosity of the host phase. The expressions of the stiffnesses are

$$A = (1-\phi_0 S)K_\mathrm{s} - \frac{2}{3}N - K_\mathrm{s}/K_\mathrm{f}^\mathrm{H}Q_\mathrm{H}\phi_0 S, \tag{A-2a}$$

$$A_\mathrm{d} = (1-\phi_0 S)K_\mathrm{s}Z - \frac{2}{3}NZ - Q_\mathrm{I}R_\mathrm{H}(K_\mathrm{s}/(K_\mathrm{f}^\mathrm{H}K_\mathrm{f}^\mathrm{I}) - 1/K_\mathrm{f}^\mathrm{I}) - Q_\mathrm{I}K_\mathrm{s}/K_\mathrm{f}^\mathrm{I} + R_\mathrm{H}K_\mathrm{s}/K_\mathrm{f}^\mathrm{H} - K_\mathrm{s}, \tag{A-2b}$$

$$N = G_b, \tag{A-2c}$$

$$Q_\mathrm{H} = \frac{K_\mathrm{s}(1-\phi_0 S - K_b/K_\mathrm{s})}{1-\phi_0 S - K_b/K_\mathrm{s} + K_\mathrm{s}/K_\mathrm{f}^\mathrm{H}\phi_0 S}, \tag{A-2d}$$

$$Q_\mathrm{I} = \frac{K_\mathrm{s}(1-\phi_0 S - K_b/K_\mathrm{s})}{1-\phi_0 S - K_b/K_\mathrm{s} + K_\mathrm{s}/K_\mathrm{f}^\mathrm{I}\phi_0 S}, \tag{A-2e}$$

$$R_\mathrm{H} = \frac{K_\mathrm{s}\phi_0 S}{1-\phi_0 S - K_b/K_\mathrm{s} + K_\mathrm{s}/K_\mathrm{f}^\mathrm{H}\phi_0 S}, \tag{A-2f}$$

$$R_\mathrm{I} = \frac{K_\mathrm{s}\phi_0 S}{1-\phi_0 S - K_b/K_\mathrm{s} + K_\mathrm{s}/K_\mathrm{f}^\mathrm{I}\phi_0 S}, \tag{A-2g}$$

$$Z = R_\mathrm{H}/(\phi_0 S)(1/K_\mathrm{f}^\mathrm{H} - 1/K_\mathrm{s}) + R_\mathrm{I}/(\phi_0 S)(1/K_\mathrm{f}^\mathrm{I} - 1/K_\mathrm{s}), \tag{A-2h}$$

and

$$\rho_{00} = (1-\phi_0 S)\rho_\mathrm{s} - \phi_0\rho_{01}, \tag{A-3a}$$

$$\rho_{01} = (1-\alpha)\rho_\mathrm{f}^\mathrm{H}, \tag{A-3b}$$

$$\rho_{02} = (1-\alpha)\rho_\mathrm{f}^\mathrm{I}, \tag{A-3c}$$

$$\rho_{11} = \alpha\rho_\mathrm{f}^\mathrm{H}, \tag{A-3d}$$

$$\rho_{22} = \alpha\rho_\mathrm{f}^\mathrm{I}, \tag{A-3e}$$

where K_b and G_b are the dry-rock bulk and shear moduli, respectively; α is the tortuosity; and ρ_f^I is the density of the inclusion fluid.

The complex P- and S-wave wave numbers (k_P and k_S, respectively) are obtained with a plane-wave analysis of equation A-1 (see equations B-1–B-4 in Ba et al., 2011). Then, the complex bulk and shear moduli of the composite porous medium are

$$K_\mathrm{sat} = ((1-\phi_0(S+dS))\rho_s + \phi_0(S+dS)\rho_f)\left(\frac{\omega}{k_\mathrm{P}}\right)^2 - \frac{4}{3}G_\mathrm{sat}, \tag{A-4a}$$

$$G_\mathrm{sat} = ((1-\phi_0(S+dS))\rho_s + \phi_0(S+dS)\rho_f)\left(\frac{\omega}{k_\mathrm{S}}\right)^2, \tag{A-4b}$$

where ω is the angular frequency, and ρ_f is the effective fluid density.

In the subsequent addition, the equivalent homogeneous medium is modeled as a porous medium saturated with an effective fluid with a complex bulk modulus. This is obtained from the Gassmann equations and serves to define the bulk modulus of the host fluid in the next step. Upon completing the final iteration, which incorporates all CO_2 patches, we can determine V_P and $1/Q_\mathrm{P}$ of the partially saturated medium.

REFERENCES

Agofack, N., S. Lozovyi, and A. Bauer, 2018, Effect of CO2 on P-and S-wave velocities at seismic and ultrasonic frequencies: International Journal of Greenhouse Gas Control, **78**, 388–399, doi: 10.1016/j.ijggc.2018.09.010.

Alam, M. M., M. L. Hjuler, H. F. Christensen, and I. L. Fabricius, 2014, Petrophysical and rock-mechanics effects of CO2 injection for enhanced oil recovery: Experimental study on chalk from South Arne field, North Sea: Journal of Petroleum Science and Engineering, **122**, 468–487, doi: 10.1016/j.petrol.2014.08.008.

Alemu, B. L., E. Aker, M. Soldal, Ø. Johnsen, and P. Aagaard, 2013, Effect of sub-core scale heterogeneities on acoustic and electrical properties of a reservoir rock: A CO2 flooding experiment of brine saturated sandstone in a computed tomography scanner: Geophysical Prospecting, **61**, 235–250, doi: 10.1111/j.1365-2478.2012.01061.x.

Arts, R., O. Eiken, A. Chadwick, P. Zweigel, L. Van der Meer, and B. Zinszner, 2004, Monitoring of CO2 injected at Sleipner using time-lapse seismic data: Energy, **29**, 1383–1392, doi: 10.1016/j.energy.2004.03.072.

Ba, J., J. M. Carcione, and J. X. Nie, 2011, Biot-Rayleigh theory of wave propagation in double-porosity media: Journal of Geophysical Research: Solid Earth, **116**, B06202, doi: 10.1029/2010JB008185.

Ba, J., W. Xu, L. Y. Fu, J. M. Carcione, and L. Zhang, 2017, Rock anelasticity due to patchy saturation and fabric heterogeneity: A double double-porosity model of wave propagation: Journal of Geophysical Research: Solid Earth, **122**, 1949–1976, doi: 10.1002/2016JB013882.

Batzle, M., and Z. Wang, 1992, Seismic properties of pore fluids: Geophysics, **57**, 1396–1408, doi: 10.1190/1.1443207.

Brie, A., F. Pampuri, A. Marsala, and O. Meazza, 1995, Shear sonic interpretation in gas-bearing sands: Annual Technical Conference and Exhibition, SPE, Extended Abstracts, 701–710.

Cadoret, T., D. Marion, and B. Zinszner, 1995, Influence of frequency and fluid distribution on elastic wave velocities in partially saturated limestones: Journal of Geophysical Research: Solid Earth, **100**, 9789–9803, doi: 10.1029/95JB00757.

Carcione, J. M., H. B. Helle, and N. H. Pham, 2003, White's model for wave propagation in partially saturated rocks: Comparison with poroelastic numerical experiments: Geophysics, **68**, 1389–1398, doi: 10.1190/1.1598132.

Carcione, J. M., F. Poletto, B. Farina, and C. Bellezza, 2018, 3D seismic modeling in geothermal reservoirs with a distribution of steam patch sizes, permeabilities and saturations, including ductility of the rock frame: Physics of the Earth and Planetary Interiors, **279**, 67–78, doi: 10.1016/j.pepi.2018.03.004.

Caspari, E., T. M. Müller, and B. Gurevich, 2011, Time-lapse sonic logs reveal patchy CO2 saturation in-situ: Geophysical Research Letters, **38**, L13301, doi: 10.1029/2011GL046959.

Chadwick, A., G. Williams, N. Delepine, V. Clochard, K. Labat, S. Sturton, M. L. Buddensiek, M. Dillen, M. Nickel, A. L. Lima, and R. Arts, 2010, Quantitative analysis of time-lapse seismic monitoring data at the Sleipner CO2 storage operation: The Leading Edge, **29**, 170–177, doi: 10.1190/1.3304820.

Chapman, S., J. V. Borgomano, B. Quintal, S. M. Benson, and J. Fortin, 2021, Seismic wave attenuation and dispersion due to partial fluid saturation: Direct measurements and numerical simulations based on X-ray CT: Journal of Geophysical Research: Solid Earth, **126**, e2021JB021643, doi: 10.1029/2021JB021643.

Cheng, Y., M. Zeng, Z. Lu, X. Du, H. Yin, and L. Yang, 2020, Effects of supercritical CO2 treatment temperatures on mineral composition, pore structure and functional groups of shale: Implications for CO2 sequestration: Sustainability, **12**, 3927, doi: 10.3390/su12093927.

Cole, K. S., and R. H. Cole, 1941, Dispersion and absorption in dielectrics I. Alternating current characteristics: The Journal of Chemical Physics, **9**, 341–351, doi: 10.1063/1.1750906.

Daley, T. M., L. R. Myer, J. E. Peterson, E. L. Majer, and G. M. Hoversten, 2008, Time-lapse crosswell seismic and VSP monitoring of injected CO2 in a brine aquifer: Environmental Geology, **54**, 1657–1665, doi: 10.1007/s00254-007-0943-z.

Delle Piane, C., and J. Sarout, 2016, Effects of water and supercritical CO2 on the mechanical and elastic properties of Berea sandstone: International Journal of Greenhouse Gas Control, **55**, 209–220, doi: 10.1016/j.ijggc.2016.06.001.

Deng, W. B., L.-Y. Fu, I. B. Morozov, and Z. W. Wang, 2023, Macroscopic mechanical properties of fluid saturated sandstone at variable temperatures: Geophysics, **88**, no. 3, MR127–MR139, doi: 10.1190/geo2022-0427.1.

Deng, W. B., L.-Y. Fu, Z. W. Wang, W. T. Hou, and T. C. Han, 2024, Biot-consistent framework for wave propagation with macroscopic fluid and thermal effects: Geophysical Journal International, **235**, 1218–1227, doi: 10.1093/gji/ggad293.

Dutta, N. C., and H. Odé, 1979, Attenuation and dispersion of compressional waves in fluid-filled porous rocks with partial gas saturation (White model) — Part I: Biot theory: Geophysics, **44**, 1777–1788, doi: 10.1190/1.1440938.

Falcon-Suarez, I., G. Papageorgiou, A. Chadwick, L. North, A. I. Best, and M. Chapman, 2018, CO2-brine flow-through on an Utsira Sand core sample: Experimental and modelling. Implications for the Sleipner storage field: International Journal of Greenhouse Gas Control, **68**, 236–246, doi: 10.1016/j.ijggc.2017.11.019.

Falcon-Suarez, I. H., M. D. Mangriotis, G. Papageorgiou, and N. H. Mondol, 2024, Impact of fluid distribution and petrophysics on geophysical signatures of CO2 storage sandstone reservoirs: Journal of Geophysical Research: Solid Earth, **129**, e2024JB029027, doi: 10.1029/2024JB029027.

Falcon-Suarez, I. H., G. Papageorgiou, Z. Jin, A. Muñoz-Ibáñez, M. Chapman, and A. I. Best, 2020, CO2-brine substitution effects on ultrasonic wave propagation through sandstone with oblique fractures: Geophysical Research Letters, **47**, e2020GL088439, doi: 10.1029/2020GL088439.

Foroutan, M., E. Ghazanfari, and A. Amirlatifi, 2021, Variation of failure properties, creep response and ultrasonic velocities of sandstone upon injecting CO2-enriched brine: Geomechanics and Geophysics for Geo-Energy and Geo-Resources, **7**, 1–30, doi: 10.1007/s40948-021-00223-y.

Gassmann, F., 1951, Über die elastizität poröser medien: Veirteljahrsschrift der Naturforschenden Gesellschaft in Zürich, **96**, 1–23.

Han, D. H., M. Sun, and J. Liu, 2012, Velocity and density of CO2-oil miscible mixtures: 82nd Annual International Meeting, SEG, Expanded Abstracts, doi: 10.1190/segam2012-1242.1.

Hangx, S., E. Bakker, P. Bertier, G. Nover, and A. Busch, 2015, Chemical-mechanical coupling observed for depleted oil reservoirs subjected to long-term CO2-exposure — A case study of the Werkendam natural CO2 analogue field: Earth and Planetary Science Letters, **428**, 230–242, doi: 10.1016/j.epsl.2015.07.044.

Hangx, S., A. van der Linden, F. Marcelis, and A. Bauer, 2013, The effect of CO2 on the mechanical properties of the Captain Sandstone: Geological storage of CO2 at the Goldeneye field (UK): International Journal of Greenhouse Gas Control, **19**, 609–619, doi: 10.1016/j.ijggc.2012.12.016.

Hill, R., 1963, Elastic properties of reinforced solids: some theoretical principles: Journal of the Mechanics and Physics of Solids, **11**, 357–372, doi: 10.1016/0022-5096(63)90036-X.

Jiang, Y., Y. Luo, Y. Lu, C. Qin, and H. Liu, 2016, Effects of supercritical CO2 treatment time, pressure, and temperature on microstructure of shale: Energy, **97**, 173–181, doi: 10.1016/j.energy.2015.12.124.

Jin, Z., M. Chapman, and G. Papageorgiou, 2018, Frequency-dependent anisotropy in a partially saturated fractured rock: Geophysical Journal International, **215**, 1985–1998, doi: 10.1093/gji/ggy399.

Kim, J., T. Matsuoka, and Z. Xue, 2011, Monitoring and detecting CO2 injected into water-saturated sandstone with joint seismic and resistivity measurements: Exploration Geophysics, **42**, 58–68, doi: 10.1071/EG11002.

Kitamura, K., Z. Xue, T. Kogure, and O. Nishizawa, 2014, The potential of V_S and V_P-V_S relation for the monitoring of the change of CO2-saturation in porous sandstone: International Journal of Greenhouse Gas Control, **25**, 54–61, doi: 10.1016/j.ijggc.2014.03.013.

Kuteynikova, M., N. Tisato, R. Jänicke, and B. Quintal, 2014, Numerical modeling and laboratory measurements of seismic attenuation in partially saturated rock: Geophysics, **79**, no. 2, L13–L20, doi: 10.1190/geo2013-0020.1.

Lebedev, M., M. Pervukhina, V. Mikhaltsevitch, T. Dance, O. Bilenko, and B. Gurevich, 2013, An experimental study of acoustic responses on the injection of supercritical CO2 into sandstones from the Otway Basin: Geophysics, **78**, no. 4, D293–D306, doi: 10.1190/geo2012-0528.1.

Le Guen, Y., F. Renard, R. Hellmann, E. Brosse, M. Collombet, D. Tisserand, and J. P. Gratier, 2007, Enhanced deformation of limestone and sandstone in the presence of high fluids: Journal of Geophysical Research: Solid Earth, **112**, B05421, doi: 10.1029/2006JB004637.

Lei, X., and Z. Xue, 2009, Ultrasonic velocity and attenuation during CO2 injection into water-saturated porous sandstone: Measurements using difference seismic tomography: Physics of the Earth and Planetary Interiors, **176**, 224–234, doi: 10.1016/j.pepi.2009.06.001.

Lemmon, E., M. McLinden, and D. Friend, 2012, Thermophysical Properties of Fluid Systems: NIST Chemistry WebBook, **69**, NIST Standard Reference Database, http://webbook.nist.gov.

Li, H., D. Wang, J. Gao, M. Zhang, Y. Wang, L. Zhao, and Z. Yang, 2020, Role of saturation on elastic dispersion and attenuation of tight rocks: An experimental study: Journal of Geophysical Research: Solid Earth, **125**, e2019JB018513, doi: 10.1029/2019JB018513, accessed 16 April 2025.

Li, J., C. Liner, P. Geng, and J. Zeng, 2013, Convolutional time-lapse seismic modeling for CO2 sequestration at the Dickman oilfield, Ness County, Kansas: Geophysics, **78**, no. 3, B147–B158, doi: 10.1190/geo2012-0159.1.

Li, N. Q., I. B. Morozov, L.-Y. Fu, and W. B. Deng, 2024, Unified nonlinear elasto-visco-plastic rheology for bituminous rocks at variable pressure and temperature: Journal of Geophysical Research: Solid Earth, **130**, e2024JB029295, doi: 10.1029/2024JB029295.

Liu, S. B., T. C. Han, and L.-Y. Fu, 2021, Laboratory investigations of acoustic anisotropy in artificial porous rock with aligned fractures during gas hydrate formation and dissociation: Journal of Geophysical Research: Solid Earth, **126**, e2021JB021678, doi: 10.1029/2021JB021678.

Liu, S. B., T. C. Han, and L.-Y. Fu, 2022, Laboratory insights into the effects of methane hydrate on the anisotropic joint elastic-electrical properties in fractured sandstones: Petroleum Science, **20**, 803–814, doi: 10.1016/j.petsci.2022.09.007.

Masson-Delmotte, V., P. Zhai, H. O. Pörtner, D. Roberts, J. Skea, and P. R. Shukla, 2022, Global Warming of 1.5 C: IPCC special report on impacts of global warming of 1.5 C above pre-industrial levels in context of strengthening response to climate change, sustainable development, and efforts to eradicate poverty: Cambridge University Press.

Mavko, G., and D. Jizba, 1991, Estimating grain-scale fluid effects on velocity dispersion in rocks: Geophysics, **56**, 1940–1949, doi: 10.1190/1.1443005.

Mavko, G., T. Mukerji, and J. Dvorkin, 2009, Rock physics handbook — Tools for seismic analysis in porous media: Cambridge University Press.

Mikhaltsevitch, V., M. Lebedev, and B. Gurevich, 2014, Measurements of the elastic and anelastic properties of sandstone flooded with supercritical CO2: Geophysical Prospecting, **62**, 1266–1277, doi: 10.1111/1365-2478.12181.

Mohapatra, A., C. S. Rai, C. H. Sondergeld, and T. Richards, 2019, Laboratory study of ultrasonic velocity variations during CO2 flooding in Tuscaloosa sandstone: SPE Reservoir Evaluation & Engineering, **22**, 520–530, doi: 10.2118/159515-PA.

Müller, T. M., B. Gurevich, and M. Lebedev, 2010, Seismic wave attenuation and dispersion resulting from wave-induced flow in porous rocks — A review: Geophysics, **75**, no. 5, A147–A164, doi: 10.1190/1.3463417.

Müller, T. M., J. Toms-Stewart, and F. Wenzlau, 2008, Velocity-saturation relation for partially saturated rocks with fractal pore fluid distribution: Geophysical Research Letters, **35**, L09306, doi: 10.1029/2007GL033074.

Nakagawa, S., T. J. Kneafsey, T. M. Daley, and B. M. Freifeld, 2013, Laboratory seismic monitoring of supercritical CO2 flooding in sandstone cores using the split Hopkinson resonant bar technique with concurrent X-ray computed tomography imaging: Geophysical Prospecting, **61**, 254–269, doi: 10.1111/1365-2478.12027.

Papageorgiou, G., I. Falcon-Suarez, M. Chapman, and A. Best, 2018, Pressure-varying CO2 distribution affects the ultrasonic velocities of synthetic sandstones: International Journal of Greenhouse Gas Control, **74**, 1–8, doi: 10.1016/j.ijggc.2018.03.022.

Schrag, D. P., 2007, Preparing to capture carbon: Science, **315**, 812–813, doi: 10.1126/science.1137632.

Sheng, B. L., T. C. Han, and L.-Y. Fu, 2024, Distribution of gas hydrate in fractured reservoirs: implications from anisotropic elastic and electrical numerical simulations: Geophysical Journal International, **237**, 838–848, doi: 10.1093/gji/ggae076.

Shi, J.-Q., Z. Xue, and S. Durucan, 2007, Seismic monitoring and modelling of supercritical CO2 injection into a water-saturated sandstone. Interpretation of P-wave velocity data: International Journal of Greenhouse Gas Control, **1**, 473–480, doi: 10.1016/S1750-5836(07)00013-8.

Siggins, A. F., 2006, Velocity-effective stress response of CO2-saturated sandstones: Exploration Geophysics, **37**, 60–66, doi: 10.1071/EG06060.

Siggins, A. F., M. Lwin, and P. Wisman, 2010, Laboratory calibration of the seismo-acoustic response of CO2 saturated sandstones: International Journal of Greenhouse Gas Control, **4**, 920–927, doi: 10.1016/j.ijggc.2010.06.007.

Sun, C., J. Fortin, J. V. Borgomano, S. Wang, G. Tang, T. Bultreys, and V. Cnudde, 2022, Influence of fluid distribution on seismic dispersion and attenuation in partially saturated limestone: Journal of Geophysical Research: Solid Earth, **127**, e2021JB023867, doi: 10.1029/2021JB023867.

Thomas, D. C. and S. M. Benson, eds., 2005, Carbon dioxide capture for storage in deep geologic formations-results from the CO_2 capture project: Vol 1 — Capture and separation of carbon dioxide from combustion, Vol 2 — Geologic storage of carbon dioxide with monitoring and verification: Elsevier.

Tisato, N., and B. Quintal, 2013, Measurements of seismic attenuation and transient fluid pressure in partially saturated Berea sandstone: Evidence of fluid flow on the mesoscopic scale: Geophysical Journal International, **195**, 342–351, doi: 10.1093/gji/ggt259.

Toms, J., T. M. Müller, and B. Gurevich, 2007, Seismic attenuation in porous rocks with random patchy saturation: Geophysical Prospecting, **55**, 671–678, doi: 10.1111/j.1365-2478.2007.00644.x.

Vasco, D. W., M. Alfi, S. A. Hosseini, R. Zhang, T. Daley, J. B. Ajo-Franklin, and S. D. Hovorka, 2019, The seismic response to injected carbon dioxide: Comparing observations to estimates based upon fluid flow modeling: Journal of Geophysical Research: Solid Earth, **124**, 6880–6907, doi: 10.1029/2018JB016429.

Vialle, S., and T. Vanorio, 2011, Laboratory measurements of elastic properties of carbonate rocks during injection of reactive CO2-saturated water: Geophysical Research Letters, **38**, L01302, doi: 10.1029/2010GL045606.

Wang, Z., and A. Nur, 1989, Effect of CO_2 flooding on wave velocities in rocks and hydrocarbons: Society of Petroleum Engineers Reservoir Engineering, **4**, 429–436, doi: 10.2118/17345-PA.

Wood, A. B., 1941, A textbook of sound: G. Bell and Sons LTD.

Xue, Z., and X. Lei, 2006, Laboratory study of CO2 migration in water-saturated anisotropic sandstone, based on P-wave velocity imaging: Exploration Geophysics, **37**, 10–18, doi: 10.1071/EG06010.

Xue, Z., and T. Ohsumi, 2004, Seismic wave monitoring of CO2 migration in water-saturated porous sandstone: Exploration Geophysics, **35**, 25–32, doi: 10.1071/EG04025.

Yang, B., H. Wang, B. Wang, Y. Yi, C. Zhao, and G. Tian, 2023, Effect of supercritical CO2-water/brine-rock interaction on microstructures and mechanical properties of tight sandstone: Transport in Porous Media, **149**, 87–115, doi: 10.1007/s11242-022-01834-z.

Yang, J., L. Y. Fu, Y. H. Zhang, and T. C. Han, 2022, Temperature- and pressure-dependent pore microstructures by using static and dynamic moduli and their correlation: Rock Mechanics and Rock Engineering, **55**, 4073–4092, doi: 10.1007/s00603-022-02829-4.

Yin, H., J. Zhou, Y. Jiang, X. Xian, and Q. Liu, 2016, Physical and structural changes in shale associated with supercritical CO2 exposure: Fuel, **184**, 289–303, doi: 10.1016/j.fuel.2016.07.028.

Yu, H., J. Ba, J. Carcione, J. S. Li, G. Tang, X. Y. Zhang, X. Z. He, and H. Ouyang, 2014, Rock physics modeling of heterogeneous carbonate reservoirs: porosity estimation and hydrocarbon detection: Applied Geophysics, **11**, 9–22, doi: 10.1007/s11770-014-0413-9.

Yu, H., Y. Zhang, Y. Ma, M. Lebedev, S. Ahmed, X. Li, M. Verrall, A. Squelch, and S. Iglauer, 2019, CO2-saturated brine injection into unconsolidated sandstone: Implications for carbon geosequestration: Journal of Geophysical Research: Solid Earth, **124**, 10823–10838, doi: 10.1029/2018JB017100.

Yun, A., and I. Song, 2022, Pore fluid substitution effects on elastic wave propagation in Berea sandstone: Implication to seismic monitoring of CO2 geologic storage: International Journal of Greenhouse Gas Control, **115**, 103609, doi: 10.1016/j.ijggc.2022.103609.

Zhang, L., J. Ba, and J. M. Carcione, 2021, Wave propagation in infinituple-porosity media: Journal of Geophysical Research: Solid Earth, **126**, e2020JB021266, doi: 10.1029/2020JB021266.

Zhang, L., J. Ba, J. M. Carcione, and C. Wu, 2022, Seismic wave propagation in partially saturated rocks with a fractal distribution of fluid-patch size: Journal of Geophysical Research: Solid Earth, **127**, e2021JB023809, doi: 10.1029/2021JB023809.

Zhang, L., L. Gao, J. Ba, J. M. Carcione, and J. Y. Min, 2024, Joint inversion of crack properties of tight carbonates from electrical conductivity and ultrasonic velocity: Petroleum Science, **21**, 4010–4024, doi: 10.1016/j.petsci.2024.05.006.

Zhang, Y., O. Nishizawa, T. Kiyama, and Z. Xue, 2015, Saturation-path dependency of P-wave velocity and attenuation in sandstone saturated with CO2 and brine revealed by simultaneous measurements of waveforms and X-ray computed tomography images: Geophysics, **80**, no. 4, D403–D415, doi: 10.1190/geo2014-0289.1.

Zhang, Y., H. Park, O. Nishizawa, T. Kiyama, and Z. Xue, 2017, Fluid distribution effects on P-wave velocity of CO2/brine saturated rocks: A comparison study and implications for CO2 storage monitoring using seismic method: Energy Procedia, **114**, 3786–3792, doi: 10.1016/j.egypro.2017.03.1509.

Biographies and photographs of the authors are not available.